Check for updates

Flexible PTh/GQDs/TiO$_2$ composite with superior visible-light photocatalytic properties for rapid degradation pollutants†

Tong Li,‡[a] Ru Li,‡*[a] Lei Yang,[b] Rongxu Wang,[a] Rui Liu,[a] Yelin Chen,[a] Shiying Yan,*[a] Seeram Ramakrishna [c] and Yunze Long *[ad]

Flexible fiber membranes for pollutant removal have received increasing attention due to their high adsorption performance and easy recycling characteristics. However, due to the lack of environmentally friendly regeneration, some adsorption membranes have low regeneration efficiency, especially in terms of chemical adsorption, so they lack reusability. This study prepares a series of conducting polymer [PAn (polyaniline) or PPy (polypyrrole) or PTh (polythiophene)] graphene quantum dots (GQDs, the size of GQDs is about 20 nm)/TiO$_2$ ternary fiber membranes *via* a facile electrospinning method with chemical deposition. Remarkably, this creates an anatase TiO$_2$ and π-conjugated system. The combination is beneficial to the photocatalytic degradation of organic pollutants, showing synergistic promotion in both the degradation rate and the degree of decomposition. The UV-vis test shows that the combination of GQDs broadens the optical response threshold of TiO$_2$, from near ultraviolet region excitation to visible region excitation. At the same time, the conductive polymer load further reduces the energy required for photogenerated electron transfer, which theoretically improves the degradation effect. Photocatalytic degradation tests showed that the PTh/GQDs/TiO$_2$ fiber membrane exhibited significant high photocatalytic activity of visible-light in the methylene blue (MB) and TC degradation. The degradation rate level is 92.90% and 80.58%, respectively and the MB removal is more than 4 times that of bare TiO$_2$ membrane. After photocatalytic regeneration four times, the regeneration efficiency can be maintained above 95%. Notably, various experimental results show that the interface charge transfer mechanism between GQDs/TiO$_2$ and PTh follows the Z-scheme heterojunction, which maximizes the retention of strong reducing electrons and oxidation holes. In the degradation, the active species of ·O$_2^-$ and ·OH, make different contributions in the photocatalysts, which oxidize and break down the pollutant molecules into small molecules and then to harmless substances. According to the electronegativity difference of the material itself, PTh acts as electron acceptor in the degradation system, and TiO$_2$ fiber membrane doped with GQDs acts as electron donor. The present research, not only offers feasibility of the PTh/GQDs/TiO$_2$ flexible fiber membrane as an environment-friendly catalyst, but also motivates researchers to develop flexible fiber materials for future photocatalytic technology.

[a]Collaborative Innovation Center for Nanomaterials & Devices, College of Physics, Qingdao University, Qingdao 266071, China. E-mail: liruouc@163.com; ysy5954418@163.com; yunze.long@qdu.edu.cn; Tel: +86 13953290681

[b]Research Center for Intelligent & Wearable Technology, College of Textiles & Clothing, Qingdao University, Qingdao 2266071, China

[c]Center for Nanofibers & Nanotechnology, Faculty of Engineering, National University of Singapore, Singapore

[d]State Key Laboratory of Bio-Fibers & Eco-Textiles (Qingdao University), Qingdao 266071, China

† Electronic supplementary information (ESI) available. See DOI: https://doi.org/10.1039/d2ra07084g

‡ These two authors contributed equally to this work.

1 Introduction

By the fast development of human society the contamination of water resources is getting out of hand. The survival and reproduction of human beings are closely related to water, so this issue has created widespread concern.[1] Organic pollutants in water seriously threaten the stability of the ecosystem and human health. Hence, in recent years researchers have discovered many ways to treat water pollution, such as photocatalysis,[2] biological treatment,[3] and adsorption.[4] Photocatalysis is one of the most attractive options because of its expediency and recyclability.[5–7] Hence, the preparation of photocatalysts with high catalytic capacity and wider selection that are green,

recyclable, and reusable is imminent.[8] Titanium dioxide (TiO$_2$) has strong oxidation, environmental protection, chemical stability, and applications in several fields, for instance artificial photosynthesis, water treatments, and other photocatalytic processes.[9] Nevertheless, two important factors affecting the photocatalytic application of TiO$_2$, namely the rapid photo-generated electron–hole recombination and the difficulty being excited by visible-light, which limits the practical application of TiO$_2$. Therefore, a variety of methods to improve the catalytic performance of titanium dioxide have been studied, such as the construction of heterojunction,[10–12] the manufacture of defects,[13] and the regulation of morphology,[14] to inhibit the photoelectron-hole recombination and increase carrier life. For example, Hossein, *et al.*[15] prepared an N-GQDs (graphene quantum dots)/TiO$_2$ nanocomposite for removal of methylene blue (MB) from water. Porous melamine sponge/TiO$_2$/PPy monoliths were obtained to create photocatalytic degradation of methyl orange (MO).[16]

Nevertheless, the above mentioned photocatalysts are typically utilized as suspended particles or slurries in reactors. Aggregation of nanocatalysts without needing to the stable support, had devoted much efforts for their separation and recovery, which is limited in practical applications.[17,18] Indeed, the recovery of the catalyst powders from the reaction systems is technically problematic. Therefore, the immobilization of photocatalysts on membranes or fiber substrates has attracted much consideration as it facilitates separation and recovery of the catalysts.[19–22]

Electrospinning as a powerful technique used to provide polymeric nanofibers with catalyst because of its simplicity as well as scalability, cost-effective, intrinsic porosity, and flexibility.[23,24] Meanwhile, the electrospun fiber can be employed as a suitable support for uniform dispersion of the catalyst.[25,26] Like a series of electrospun fiber of Cu$_2$O/Bi$_2$O$_2$CO$_3$, Wang *et al.* synthesized heterojunctions by a developed electrospinning technology.[27] Zhang *et al.* fabricate PAN/β-CD/TiO$_2$/GO composite nanofibrous membrane photocatalysts using electrospinning technique accompanied by ultrasonic-assisted electrospray deposition.[28] Photocatalytic technique has been widely considered as an environmentally friendly tool that could decompose target entities to nontoxic species.[29] Surprisingly, the combination of electrospinning and photocatalytic technologies leads to an easier recovery and regeneration procedure of membranes with much environmentally friendly features.

Conductive polymers are adjustable in the process of solution synthesis and have been widely used in various fields, such as solar cells,[30] supercapacitors[31] and light-emitting diodes.[32–34] Because conductive polymers can provide band structure matching with other inorganic semiconductors, by combining conductive polymers (especially polythiophene, polypyrrole and polyaniline) with semiconductor nanomaterials to prepare composite photocatalysts, on the one hand, the spectral response range of bulk materials can be broadened. On the other hand, it can improve the separation efficiency of photo-generated charge and improve the photocatalytic performance of the material.[35] Polythiophene has the characteristics of high

conductivity, small band gap and high electron mobility, which is an ideal TiO$_2$ catalyst system composites.[36]

In this work, we first proposed that the flexible graphene quantum dots (GQDs)/TiO$_2$ (GT) binary fibrous membrane was obtained by electrospinning combined with hydrothermal methods. The CPs (polyaniline, polypyrrole and polythiophene)/GT (CPs/GT) ternary flexible fibrous membrane was synthesized by polymerization, conductive polymer anchored to the GT fibrous membrane *in situ*. The photocatalytic activity of CPs/GT fiber membrane was tested by introducing MB and antibiotic tetracycline hydrochloride (TC). At the same time, the results of UV-vis, the free radical capture experiment, and the VB-XPS test showed that the interfacial charge transfer mechanism of GT and PTh followed the Z-scheme heterojunction, which maximized the redox ability of the remaining active sites, thus enhancing the photocatalytic activity of the compound. The load of conductive polymer provides more channels for photo-electron transfer, and $\cdot O_2^-$ is the primary active substance with a major role. All the results showed that GQDs and CPs effectively improved the photocatalytic performance of TiO$_2$. We discuss the impact of our findings for systematized fabrication of flexible TiO$_2$-based catalysts for energy and environmental applications.

2 Experimental section

2.1 Preparation of flexible GQDs/TiO$_2$ binary fibrous membranes

As typical procedure we prepared the GQDs/TiO$_2$ flexible membrane, by adding 4 g of polyvinylidene fluoride (PVDF) to 10 g of DMF and 10 g of acetone followed by stirring for 12 h to achieve a clear and transparent solution. Then, 10.0 mL butyl titanate (TBOT) is added to the mixture and stirred at 40 °C for 1 h to form PVDF/TBOT precursor system. The solution is electrospun at a voltage of 15 kV with an impulsion speed of 1 mL h^{-1}. The prepared membrane is washed by deionized water followed by drying procedure at 50 °C under vacuum overnight, referred as PVDF/TBOT flexible membranes. Then, the film is cut into 2 cm × 2 cm homogeneous slices and heated at 150 °C for 24 h in a reaction kettle with PTFE lining. For comparison, the amounts of GQDs added were 5, 10, 15, 20, 25, and 30 mL. The prepared samples are denoted as GT—5, GT—10, GT—15, GT—20, GT—25, and GT—30. After that, the GT—25 is abbreviated to GT.

2.2 Preparation of flexible CPs/GQDs/TiO$_2$ ternary fibrous membranes

The synthesis of flexible CPs/GQDs/TiO$_2$ (CPs/GT) fiber membranes was accomplished by *in situ* polymerization (IP) of conducting polymers on the electrospun GQDs/TiO$_2$ fibers.

PTh/GT flexible membrane was prepared through *in situ* polymerization of thiophene monomer onto the GT membrane surface, followed by an improved *in situ* oxidative polymerization procedure. A solution of thiophene monomer (10 mL) and chloroform (30 mL) was positioned in a 150 mL conical flask, and ultrasound was performed for 30 minutes. The GT film was

put in place, and then ferric chloride (1 g) dissolved in chloroform (30 mL) was dropped into the thiophene solution. The mixture was ultrasonic at 25 °C. Ultrasound was performed on an ultrasonic bath with a thermometer for 4 h. The obtained PTh/GT flexible ternary fiber film was then washed with deionized water to remove impurities and finally dried overnight in a vacuum oven at 50 °C. Molar mass ratio Ti : thiophene monomer = 1 : 2. The preparation process is shown in Scheme 1.

2.3 Dark adsorption experiments

Dark adsorption experiments were conducted in a single-component solution at room temperature.

Regarding the adsorption experiment for TC, 35 mL TC solution (20 mg L^{-1}) was added to different test tubes in the dark, and 0.067 g of different flexible films were added to the test tubes accordingly. We obtained the adsorption kinetics using extraction of solution (3 mL) for the duration of various adsorption times for concentration analysis. The analyzed solution was quickly poured back into the tube to ensure that the TC volume was roughly the same.

Based on the Lambert–Beer law,[37] the TC concentrations can be deduced by maximum absorption at 357 nm.[38] The amount of adsorption, q_t, (mg g^{-1}) at various adsorption time (t) was estimated using eqn (1):

$$q_t = \frac{C_0 - C_t}{m} V \qquad (1)$$

In this expression, C_0 (mg L^{-1}) and C_t (mg L^{-1}) denote the initial and the residual concentrations after adsorption for different times (t), respectively, V (L) refers to the volume of the solution, and m (g) is the amount of adsorbent.

2.4 Photocatalytic experiments

Photocatalysis efforts were conducted in single-component solution at 25 °C.

2.4.1 Visible-light photocatalytic experiments. Concerning photocatalysis experiments of the flexible membranes for TC degradation, a 2 cm × 2 cm sample was added in a quartz vessel containing 35 mL TC solution (20 mg L^{-1}) for 1 h adsorption in the dark. Afterward, the vessel was irradiated under visible light (an Xe lamp [300 W] with a UV cut filter [$\lambda >$ 420 nm]) for various times. The concentration was measured by drawing a 3 mL solution during experimental procedures. The analyzed solution was quickly poured back into the tube to ensure that the TC volume was roughly the same.

For photocatalytic regeneration evaluation, the photodegraded fiber film was washed with deionized water and dried overnight in a 60 °C vacuum oven. We repeated the experiment of photodegradation of TC and evaluated the photodegradation capacity of the catalyst for MB (10 mg L^{-1}) by following the same steps.

2.4.2 Free radicals scavenger test. In typical photocatalytic degradation processes, electron (e$^-$) holes (h$^+$), hydroxyl radicals (·OH) and superoxide radicals (·O$_2^-$) are active species involved in the reaction.[39,40] Free radicals trapping efforts were performed to recognize the reactive radicals, which known as the essential factors in TC degradation. Silver nitrate (AgNO$_3$), ammonium oxalate (AO), isopropanol (IPA), and p-benzoquinone (BQ) scavenger could scavenge, respectively, electron (e$^-$), hole (h$^+$), hydroxyl radical (·OH), and superoxide radical (·O$_2^-$). After the dark reaction, the scavengers were placed in TC solutions followed by performing the experiments one after another in keeping with the above mentioned route.

2.4.3 Identification of degradation intermediates. The identification of intermediates of TC was carried out by an LC-MS equipped with an Eclipse Plus C18 column (100 mm × 4.6 mm, 5 μm). Elution was conducted by 0.1% (v/v) formic acid aqueous solution (A) and acetonitrile (B) at a flow rate of 0.3 mL min^{-1}. The injection volume and the column temperature were set to 10 μL and 30 °C, respectively. The gradient elution conditions were 80% A + 20% B. MS was conducted in positive ion mode using an electrospray ionization source (ESI) under spray voltage of 3.8 kV, gas rate of 40 mL^{-1}, capillary temperature of 320 °C, and gas temperature of 300 °C. The mass range of MS scanning was set at 100–600 m/z.
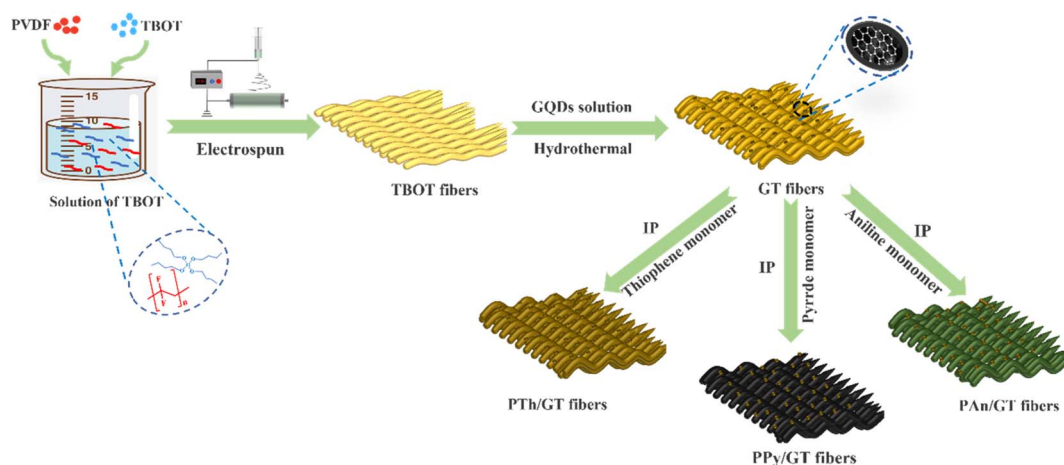
Scheme 1 Schematic diagram of the synthesis of CPs/GT flexible fiber membranes.

3 Results and discussion

3.1 Structure and morphology of flexible fiber membrane

The structural and morphological characterization of the products was conducted by XRD patterns, FTIR spectra and TEM images, as represented in Fig. 1a–d. The diffraction peaks of TiO_2 matched well with anatase TiO_2 (JCPDS no. 21-1272) (Fig. 1a).[41,42] And the diffraction peaks of XRD patterns at 27° (002) were indexed to the GQDs (Fig. S1a† shows the XRD of pure GQDs). This is consistent with the interlayer distance of the graphene sheet and shows the graphite properties of the crystallization point. Notably, a wide peak of PTh appears at 26.4°; at 25.3°, the peaks of PPy and PAn appear although the peaks of GQDs remain. A series of TiO_2, GT, PTh/GT, PPy/GT and PAn/GT fiber membranes were depicted by FTIR spectra (Fig. 1b), while the appeared peaks at $\sim$1400 cm^{-1} and $\sim$1187 cm^{-1} corresponded to the vibrational frequencies of the Ti–O–Ti and C–H groups, respectively.[43] The TiO_2 vibrations ranged around 500–850 cm^{-1} correspond to the Ti–O and O–Ti–O bonds.[44] This showed the success of electrospinning titanium dioxide fiber membrane. Different from pure TiO_2, the peak at $\sim$1600 cm^{-1} in residual photocatalyst can be attributed to the adsorbed water/OH on TiO_2.[45] These findings corroborate the existence of GQDs in the flexible sample. Compared with the infrared image of the pure conductive polymer (Fig. S1b†), the characteristic peak of doping in the infrared spectrum of PTh is $\sim$1336 cm^{-1}. The in-plane and out-of-plane bending vibrational absorption peaks for C–H bond were detected at 1020–

1200 cm^{-1} and $\sim$795 cm^{-1}, respectively. The stretching vibration absorption peak of C–S was observed at $\sim$660 cm^{-1}.[46] FTIR spectra of PAn/GT showed a benzene aromatic amine stretching vibration (C–N) peak at $\sim$1284 cm^{-1}, indicating the presence of PAn on the flexible fiber membrane surface.[47] In addition, the peaks of $\sim$1176 cm^{-1} and $\sim$1286 cm^{-1} on PPy/GT correspond to the stretching vibration peaks of C–N on PPy, and the $\sim$1554 cm^{-1} and $\sim$975 cm^{-1} peaks are attributed to the stretching vibration peak of the PPy five-element ring and the bending vibration peak of the C–H bond ring, respectively.

The surface morphology of the flexible fiber membrane was studied using TEM. The GT fiber membranes were characterized with the SAED pattern in Fig. S2a and b.† The (101) fact with the lattice spacing of TiO_2 with 0.35 nm and the (100) crystal planes of GQDs with 0.21 nm lattice spacing as observed indicated that both the TiO_2 and the GQDs particles existed in the fiber membrane. As shown in Fig. 1c and d, it is clear that the irregular floccule PTh are loaded by GT fibers on the surface (the floccule is PTh, and nanofibers are GT). The PTh/GT fibers comprised random orientation nanofibers with rough surfaces and a diameter of approximately 400 nm, which increases the active sites of the catalyst.[48] Furthermore, EDS images of PTh/GT flexible fibers (Fig. 1) demonstrated that PTh particles existed on the fiber membrane. Similarly, Fig. S2c–f† can also demonstrate the successful synthesis of other conductive polymers with GT. Notably, the resultant pure TiO_2, GT, and PTh/GT films have the same flexibility as ordinary fabrics (Fig. S2g–i†). Owing to their mechanical properties, PTh/GT membranes
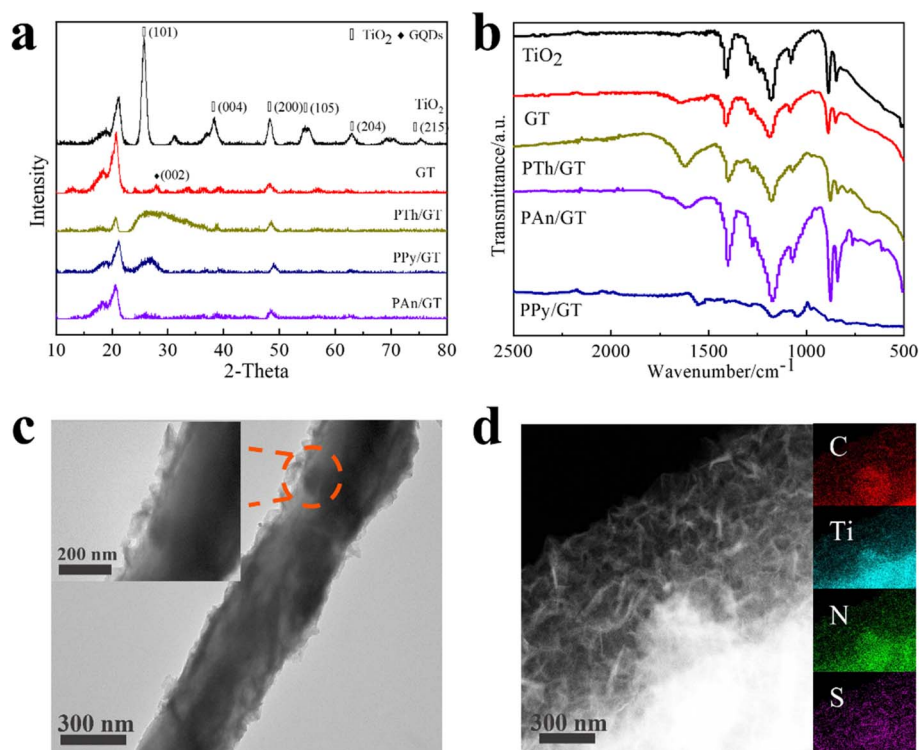

Fig. 1 (a) XRD patterns, (b) FTIR spectra of pure TiO_2 and TiO_2-based photocatalysts. (c) TEM image and (d) TEM elemental mapping image of the presence and distribution Ti, C, N and S in the PTh/GT.

demonstrate potential catalytic applications for water treatment that can easily be recovered from water through time-saving direct extracting methods. Furthermore, the color of the flexible membrane becomes dark, implying potential visible light absorption.

The XPS spectra of all the composite photocatalysts are represented in Fig. 2 and S3.† GT and the CPs/GT fiber membrane can be clearly observed from the O, Ti and C elements in Fig. S3.† In addition, because of the doping of CPs, there are more peaks of the N element in the spectra of such photocatalysts. The intensity of S 2p peak position between 163–168 eV in the XPS spectrum of PTh/GT is slightly higher than that of the GT (judged by normalized area). As shown in Fig. 2b, the two characteristic peaks of Ti $2p_{3/2}$ and Ti $2p_{1/2}$ in PTh/GT are positioned at respectively 457.9 and 463.6 eV, due to the presence of Ti^{4+} in TiO_2 fibers. Moreover, the difference in binding energy between the two peaks is 5.7 eV, and the two characteristic peaks of Ti $2p_{3/2}$ and Ti $2p_{1/2}$ of GT are located at respectively 457.6 eV and 463.4 eV according to Fig. S3b,† which is obviously offset. This phenomenon can be attributed to the fact that GQDs can extensively absorb visible light,[49] form Ti–O–C bond with TiO_2, and promote charge transfer.[50] Due to the small scale of quantum dots, the quantum scale effect under the ultra-small surface leads to the small band gap, large specific surface area and strong electrical conductivity. When GQDs is combined with TiO_2, on the one hand, the response intensity of the composite material to light can be increased, which improves the utilization efficiency of light energy of the catalyst;

on the other hand, the number of photo-generated carriers and mobility can be increased. Moreover, since the Fermi level of GQDs is lower than that of TiO_2, electrons will flow from the latter to the former until their Fermi levels match. The change in electrical properties caused by electron transfer creates a strong electric potential that causes band bending. Therefore, after coupling with GQDs, the edge of TiO_2 band will move.[51] The positive shift of binding energy confirms the transfer of charge from GT to PTh/GT, forming a strong interaction.[52] Fig. 2d is a high-resolution image of S. The peak of S $2p_{1/2}$ and S $2p_{3/2}$ indicates that thiophene monomers are not destroyed during polymerization into polythiophene.[53] The PTh improves the interaction between each component, which is conducive to improving the photoelectric chemical properties of the ternary composite. The XPS peak data diagram of PPy/GT and PAn/GT is shown in Fig. S4.† Meanwhile, the element composition and atomic percentage of the ternary composite catalyst are shown in Table S1.†

3.2 Dark adsorption performance

The flexible hybrid fiber membrane adsorbed TC solution (initial concentration of 20 mg L^{-1}) to characterize its dynamic adsorption performance (Fig. 3a). At the beginning step of the adsorption process, the flexible fiber membrane showed good adsorption performance and could quickly adsorb TC pollutants into the system. With the passage of time, the adsorption system reached equilibrium after 1 h. To understand the rate-
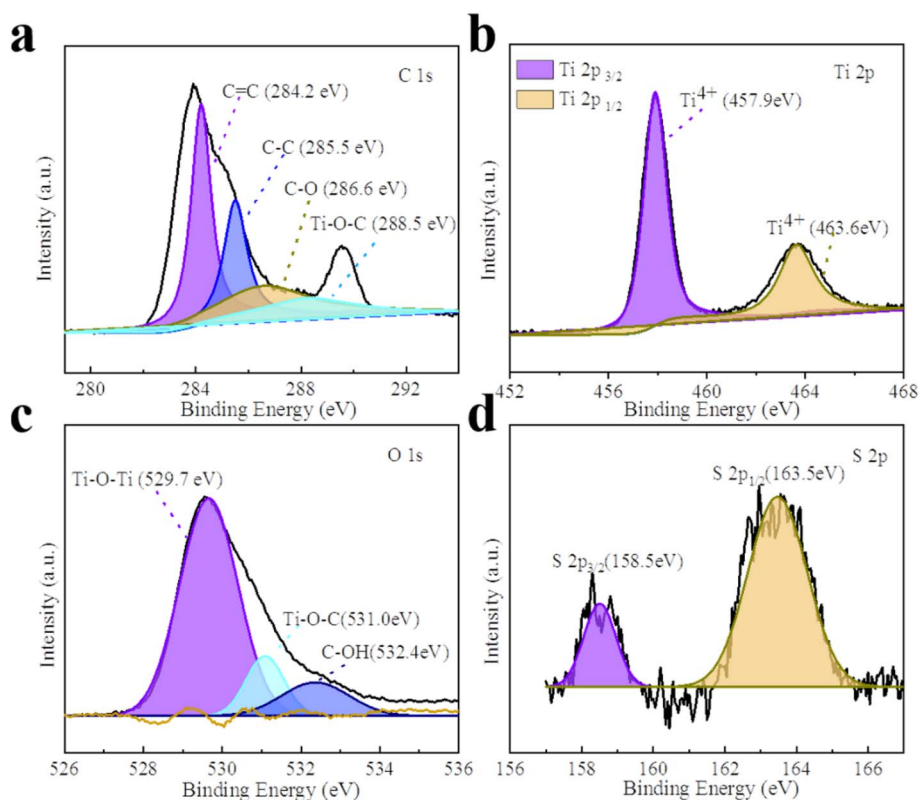

Fig. 2 XPS spectrum of PTh/GT. (a) C 1s, (b) Ti 2p, (c) O 1s, (d) S 2p.
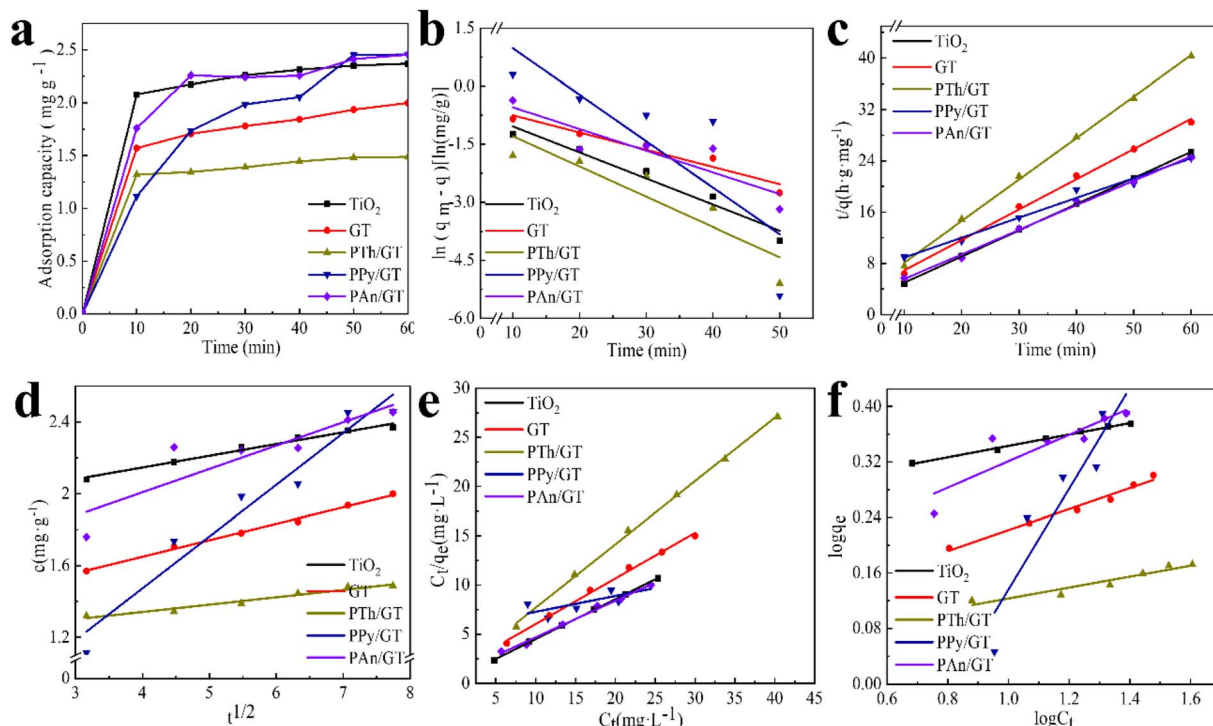
Fig. 3 (a) The influence of reaction time on TC adsorption. (b) Pseudo-first-order model, (c) pseudo-second-order model, (d) intra-particle diffusion, (e) Langmuir and (f) Freundlich isothermal model.

limiting step and adsorption mechanism, the experimental findings were evaluated by pseudo-first-order,[54,55] pseudo-second-order,[56] intra-particle diffusion kinetic models, and the Langmuir and Freundlich isothermal model. These models were presented in eqn (2)–(6):[3]

$$\ln(q_e - q_t) = \ln q_e - k_1 t \quad \text{pseudo-first-order} \tag{2}$$

$$\frac{t}{q_t} = \frac{t}{q_e} + \frac{1}{k_2 q_e^2} \quad \text{pseudo-second-order} \tag{3}$$

$$q_t = k_{id} t^{1/2} + C \quad \text{intra-particle diffusion} \tag{4}$$

$$\frac{C_t}{q_e} = \frac{C_t}{q_{max}} + \frac{1}{K_L q_{max}} \quad \text{Langmuir isothermal model} \tag{5}$$

$$\log q_e = \frac{1}{n} \log C_t + \log K_F \quad \text{Freundlich isothermal model} \tag{6}$$

In the formula, the adsorption capacity of TC at equilibrium time and t time is expressed by q_e (mg g^{-1}) and q_t (mg g^{-1}), in turn. The pseudo-first-order, pseudo-second-order, and intra-particle diffusion rate constants of the flexible fiber membrane adsorption process are k_1 (min^{-1}), k_2 (g mg^{-1} min), and k_{id} (mg g^{-1} min$^{-0.5}$). c (mg g^{-1}) represents the adsorption constant. The residual concentration of TC in the catalytic system after t adsorption time was expressed by C_t (mg L^{-1}); the maximum adsorption capacity of catalyst is prepared on the q_{max} (mg g^{-1}) surface; K_L corresponds to binding site affinity constant; and n and K_F are Freundlich constants in correlation with adsorption strength and adsorption capacity, in that order.

The linear fitting of the pseudo-first-order/pseudo-second-order models, intra-particle diffusion, and its parameters are presented in Fig. 3b–d. Table S2† illustrates its specific parameters. Take PTh/GT for example. The pseudo-second-order model demonstrates the adsorption kinetics of TC on ternary flexible membranes (R^2 0.998 > 0.9549 > 0.7751). The adsorption process of the system is a rate-controlled process, that is, the electron sharing and conversion between catalyst and pollutant.[57] It can be found from Fig. 3e, f and Table S3,† compared with Freundlich model, the Langmuir isothermal model has a better fit level with the obtained data, implying primarily chemical interactions between TC and the flexible fiber membrane surface, in good agreement with the exhibited kinetic adsorption.

3.3 Light absorption properties

The light absorption abilities of flexible membrane photocatalysts were studied with UV-vis DRS analyses (see Fig. 4a). The resultant band gaps are demonstrated in Fig. 4b. Pristine TiO$_2$ fibrous membrane is responsible just to UV light. This is consistent with the inherent absorption characteristics of pure TiO$_2$, whose absorption edge is close to 380 nm, corresponding to its band gap of 3.47 eV (Fig. S5†). After the composite GQDs, the composite fiber film showed a significant increase in absorption and a small amount of red shift in the visible region, indicating that GQDs can broaden the response range of TiO$_2$ to visible and near-infrared light (Fig. S5a†).[58] Notably, the CPs/GT flexible fiber membrane exhibited an apparent improved response in the visible region, attributed to the robust visible-
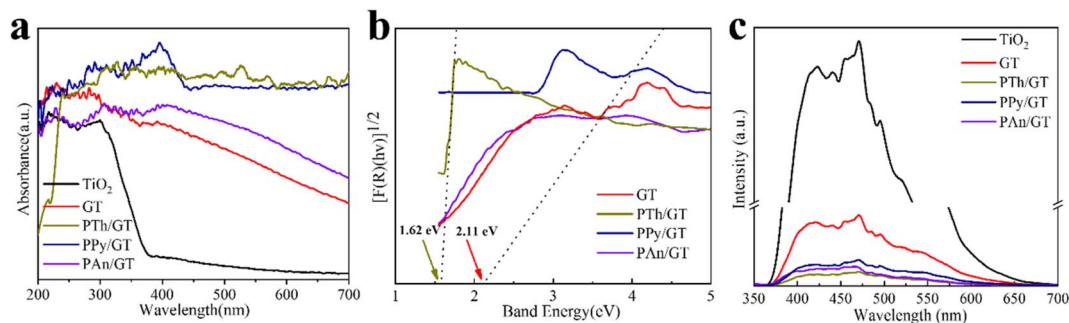
Fig. 4 (a) The UV-vis DRS, (b) E_g and (c) PL spectra of TiO$_2$-based photocatalysts.

light absorption facility of coupled CPs. In addition, the band gaps energy (E_g) of TiO$_2$-containing fiber membrane photocatalysts could be evaluated by the Kubelka–Munk equations (eqn (7) and (8)):[59]

$$F(R_\infty(\lambda)) = \frac{(1 - R_\infty)^2}{2R_\infty} \quad (7)$$

$$R_\infty = \frac{R}{R_{BaSO_4}} \quad (8)$$

In these expressions, R and R_{BaSO_4} denote the reflectance recorded for a sample and for a reference, respectively. The band-gap energy (E_g) can be determined by converting the Kubelka–Munk equations to the $(F(R_\infty)E)^{1/2}$ form, accompanied with changing of the wavelength into energy units (eV). The E_g is measured using the extrapolation technique. As illustrated in Fig. 4b and S5b,† the obtained E_g of PTh/GT fiber membrane were found to be 1.62 eV, smaller than that of pristine GQDs powder (1.66 eV), GT fiber membrane (2.11 eV), and TiO$_2$ (3.47 eV),[60] which indicated that the PTh/GT fiber membrane had better photo-absorption performance and better matching energy band structure to address pollutants under visible light irradiation.[61,62]

The electron–hole recombination efficiency of photocatalyst was characterized by PL spectroscopy.[63] The lower the excitation intensity, the lower the recombination efficiency of electron–hole photogeneration, resulting in higher photocatalytic performance.[64] As is displayed in Fig. 4c and S5d,† PTh/GT flexible fiber membrane has the lowest spectral intensity, which enables increased photocatalytic efficiency, which has also been verified in the later experiment.

3.4 Photocatalytic experiments and reusability

The CPs/GT flexible fiber membranes have the advantages of the small band gaps, superb porosity characteristics, and fast separation of the e$_{CB}^-$–h$_{VB}^+$ pairs. These make them potent materials for exceptional visible-light photocatalytic activity in the organic contaminants degradation. We studied the visible-light photocatalytic activity of the composite flexible fiber membranes in relation to the degradation of two harmful organic pollutants, MB and TC. Simultaneously, for better comparison, we also tested as-prepared pure TiO$_2$ and a series of GT in the identical conditions (Fig. 5a, b and S6†). The results

indicate that the CPs/GT fiber membranes show much higher photocatalytic activity than those with pure TiO$_2$ and binary GT catalysts. The effects of composite GQDs and various CPs on the visible light degradation of organic dyes and representative antibiotics TC were studied in detail. It should be added that the pH value of the organic dye MB solution is 9.1 and that of the antibiotic TC solution is 4.5, which fully takes into account the degradation of pollutants in the weak acid and base environment and is more in line with the actual environmental application.

The kinetics of photocatalytic degradation of MB with different catalysts is shown in Fig. S6† clearly, the degradation efficiency of GQDs composite binary film is significantly higher than that of pure TiO$_2$ film, and GT has the highest degradation efficiency. With the further increase of the recombination amount of GQDs, the photocatalytic performance decreases, which may be due to the agglomeration of excessive catalysts on the same carrier surface, resulting in the coverage of some active sites and thus affecting the photocatalytic performance.[65] The chemisorption of GQDs on TiO$_2$ and the possible formation of a C–O–Ti bond are responsible for the effective charge transfer at the interface and improved photocatalytic activity of the samples.[66] It is worth noting that PPy/GT degrades MB most efficiently. The difference in removal of different pollutant systems may be related to the different structural properties of the pollutants, which has a great influence on the direct bonding and electrostatic interaction between the pollutant and the photocatalyst.[67]

We investigated the photocatalytic performance of the flexible membrane in TC, including the degradation efficiency and kinetic characteristics; and the results are shown in Fig. 5. The system was placed at dark medium for 1 h to reach the adsorption equilibrium state. Fig. 5a shows that TiO$_2$ fiber has almost no photocatalytic activity to tetracycline under visible light irradiation for 150 minutes whereas the activity of PTh/GT, PPy/GT, and PAn/GT is significantly increased. The degradation rates of PTh/GT hybrid fiber membranes were respectively 4.06 and 1.70 times greater than those of TiO$_2$ and GT. For PTh/GT hybrid fiber membrane, its photo-degradation efficiency for MB and TC are as great as 92.90% and 80.58%.

It can be determined that PTh/GT flexible hybrid fiber membrane has the highest photocatalytic activity and degradation efficiency for TC (Fig. 5b). To accomplish the TC
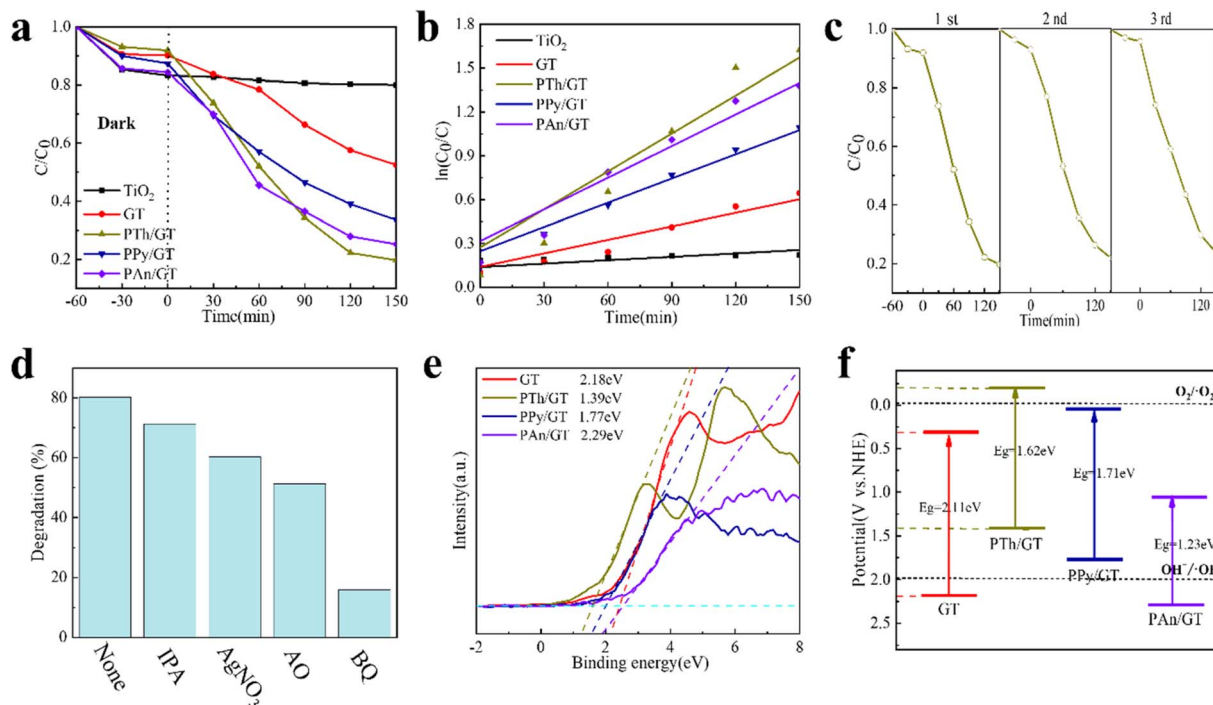
Fig. 5 Photocatalytic degradation of TC for various catalysts. (a) The relative concentration (C/C_0) of TC in various catalysts as a function of irradiation time up to 150 min. (b) Plot of $\ln(C/C_0)$ *vs.* irradiation time (t) for TC degradation in various catalysts. (c) The relative concentration of TC as a function of irradiation time for PTh/GT catalyst for three repeated cycles. (d) Degradation (%) of TC without quencher and in presence of scavengers. (e) VB XPS, (f) band structure of catalyst.

degradation reaction kinetics, the kinetic data of the photocatalytic reaction were fitted by the Langmuir–Hinshelwood kinetics pattern ($\ln[C_0/C_t] = kt$, in which C_0 and C_t are the concentrations of TC aqueous media at $t = 0$ and t minutes of the photocatalytic reaction).[68] It is found from Fig. 5b, that the model demonstrates pseudo-first-order reaction kinetics. PTh/GT displays a high catalytic activity in the degradation of TC with a reaction rate constant of 0.0087 min^{-1}, which is 1.24-fold, 1.53-fold, and 2.9-fold higher than that of PAn/GT (0.007 min^{-1}), PPy/GT (0.0057 min^{-1}), and GT (0.003 min^{-1}), respectively. The same trend was observed for MB degradation, which demonstrates the reaction rate constant of PTh/GT (0.011 min^{-1}) and PAn/GT (0.01 min^{-1}), PPy/GT (0.017 min^{-1}), and GT (0.009 min^{-1}). This finding supplementary approves that the photocatalytic activity of the tricatalyst CPs/GT is far superior to that of the binary GT catalyst. Amongst the diverse conducting polymers, PTh exhibits the highest absorption coefficient and widest absorption wavelength in the visible region of the spectra, which can improve semiconducting oxide-based photocatalysts harvesting the solar light effectively.[69] Furthermore, the lowest unoccupied molecular orbital (LUMO)-highest occupied molecular orbital (HOMO) gaps of 1.95 eV are lower than PPy (2.50 eV) and PAn (2.10 eV).[70–72] The smaller HOMO–LUMO gaps lead to more photons absorption by PTh/GT under visible light irradiation as well as their favorable photocatalytic performance under visible light. Hence, the photocatalytic activities on degraded TC of CPs/GT composites follow the hierarchy of PTh/GT > PAn/GT > PPy/GT.

We investigated the reusability of hybrid fiber membrane doped with conductive polymer for TC and MB degradation. Fig. 5c shows the relative concentration of TC in the PTh/GT flexible hybrid fiber membrane catalyst for three repeated photocatalytic cycles. It is clear that PTh/GT catalysts are stable in three repeat cycles, and the degradation effect of TC is only reduced by 4% after three cycles. However, PPy/GT and PAn/GT composite catalysts were relatively stable, and their degradation effects were 7% and 6% lower in three cycles of degradation, respectively (Fig. S7†). Meanwhile, when MB is selected as the pollutant, after four cycles, the cycling effect of PTh/GT is the best, only decreasing by 2.9% (Fig. S8†). In addition, in order to evaluate the structural stability of the catalyst, we recorded the XRD and TEM spectra of the samples before and after the catalytic cycle. Fig. S9a† is the XRD pattern of PTh/GT before and after catalysis. The results showed that the crystal phases of TiO$_2$ and PTh did not change even after three repeated photocatalysis. Moreover, the morphology of PTh/GT were similar to those of fresh samples, which further confirms the stability of PTh/GT for repeated use (Fig. S9b and c†). Compared with other polymers, PTh has the advantages of high environmental stability, structural diversity, a wide range of light absorption, high conductivity,[36] and a cycling effect.

To evaluate the contributing visible light in photocatalytic activity, we conducted a series of free radical scavenging experiments on PTh/GT hybrid fiber membrane catalysts (Fig. 5d). As seen in Fig. 5d, the degradation efficiency decreased with the addition of any trapping agent, suggesting that all oxidizing species contribute to the degradation of TC.

Significantly, it was shown a high extinguishing of TC degradation in the presence of BQ (16.8%). Our findings reveal the important role of the superoxide radical ($\cdot O_2^-$) in TC degradation. In addition, AO scavenger investigations demonstrate the second uppermost quenching of TC degradation, which indicates that the hole (h^+) is the second active substance for TC degradation. On the one hand, photogenic holes are the source of $\cdot OH$ radicals in photocatalysis; on the other hand, electrons from GQDs are transferred to the TiO_2 conduction band, where they capture O_2 and convert it to $\cdot O_2^-$.

Furthermore, from the VB XPS measurements (Fig. 5e), the valence band maximum was estimated to be 2.18, 1.39, 1.77, and 2.29 eV for GT, PTh/GT, PPy/GT, and PAn/GT, respectively. These data are helpful for further study of the photocatalytic mechanism. As shown in Fig. 5f, the E_{CB} value of PTh/GT becomes negative in comparison to GT, which implies the stronger reduction of PTh/GT than GT. In addition, e^- on the CB level of the PTh/GT can convert O_2 to $\cdot O_2^-$ due to more negative E_{CB} of PTh/GT than the redox potential of $O_2/\cdot O_2^-$ (−0.046 eV $vs.$ NHE).[63] The VB edge potential of GT is greater than $OH^-/\cdot OH$ (+1.99 eV $vs.$ NHE).[73] Hence, there are two main ways of $\cdot OH$ generation in the system: the hole oxidation of GT and the reaction between $\cdot O_2^-$ and H^+ generated on the LUMO of PTh.

The prepared PTh/GT was compared to other reported photocatalysts. The results are shown in Table S4.† Under visible light, on the degradation efficiency of TC, the PTh/GT catalyst obtained in this study is better than other photocatalysts prepared by previous studies. On the whole, the flexible hybrid fiber membrane catalyst prepared here has a high degradation efficiency of TC pollutants under visible light. Therefore, it has greater value in practical application.

3.5 Analysis of TOC and possible TC photodegradation intermediates

The main components after TC degradation were confirmed by TOC analysis (Fig. 6). Obviously, with the passage of time, TOC concentration in TC solution decreases continuously (Fig. 6a).

When the photocatalytic reaction time is 150 minute, the degradation rate of TC and the mineralization rate of TOC are 80.58% and 29.1%, respectively; and after 210 minute, the mineralization rate of TOC is 36.9% (Fig. 6b). The results show that in the photocatalytic process, the pollutants of large molecules are first decomposed into small organic molecules and then decomposed into inorganic substances, CO_2 and water. Intermediate products after TC degradation are often detected by LC-MS. Fig. S10† represents the MS mass spectrogram and the speculated product molecular formula after the degradation of TC pollutant for 120 minute. Based on the detection results, two possible degradation paths of TC were deduced and explicated in the PTh/GT system (Fig. S11†). Path 1 shows the degradation process of TC hydroxylation. TC was converted into TC1 and TC2 by hydroxylation,[74] and then the C=O in TC2 was broken by $\cdot OH$ to become TC3. The gradual degradation of TC is shown by pathway 2. When TC is attacked by free radicals such as $\cdot O_2^-$ and $\cdot OH$, the reactions of dehydroxylation, denitrification, deacetylation, and benzene ring enlightenment are produced. After the reaction, intermediates are mineralized into inorganic substances such as CO_2 and H_2O.[75]

3.6 Photocatalytic activity interpretation and reaction

Transient photocurrent response is related to the separation efficiency of photogenerated e^-–h^+ in the duration of the photoreactions. Fig. 7a shows and compares the transient photocurrent responses of GT, PTh/GT, PPy/GT, and PAn/GT photocatalysts with several on–off cycles of intermittent illumination. The figure shows that the photocurrent density of all the systems reach to a constant value for the ON state (turn on). However, the photocurrent density rapidly drops to zero in the OFF state (turn off), showing good reproducibility of all systems. The PTh/GT photocatalyst demonstrates a highest photocurrent density, indicating that the PTh/GT photocatalyst is vigorous in generating e^-–h^+ and transferring electrons. In particular, the stable photocurrent density value of the PTh/GT photocatalyst is almost 1.9 times higher than that of GT. After the incorporation
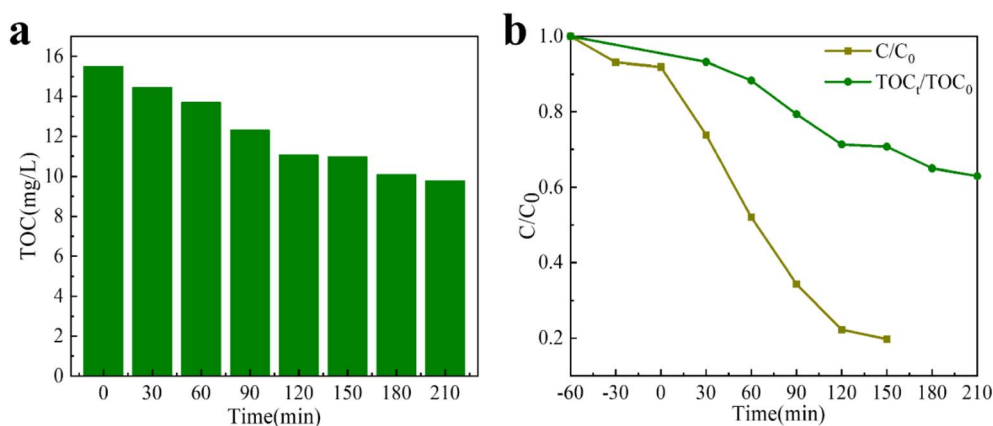

Fig. 6 (a) The TOC concentration of TC solution at various time. (b) Comparison of the degradation rate of TC with the mineralization efficiency of TOC.
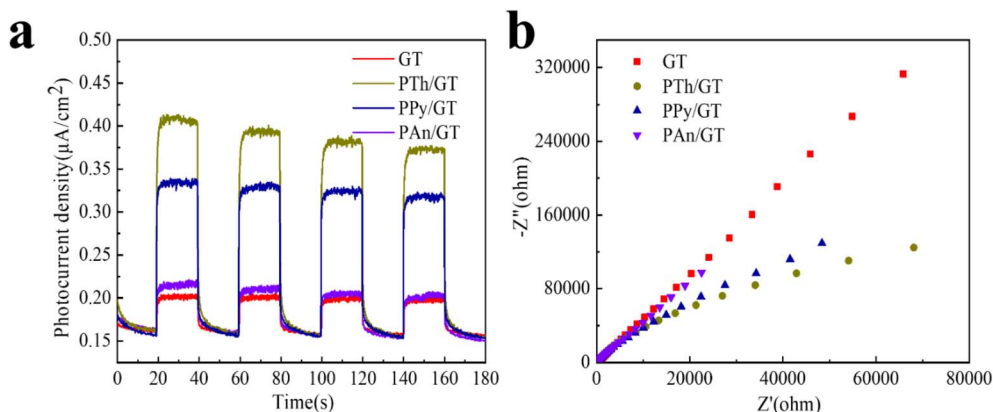
Fig. 7 (a) Transient photocurrent response and (b) electrochemical impedance spectra of TiO_2-based photocatalysts.

of conductive polymer PTh, the photocurrent intensity of PTh/GT is significantly improved. This indicates that the flexible hybrid fiber membrane has better photocatalytic performance, in agreement with the specific experimental findings. The improvement of catalytic activity is closely related to the good visible light absorption and electron transport capacity of conductive polymers.

Moreover, the electrochemical impedance spectroscopy is an effective technique for analysis of the $e^-–h^+$ separation efficiency. The larger the radius curve, the greater the resistance of electron transport.[76–78] Fig. 7b shows that the impedance of the radius CPs/GT hybrid fiber is obviously smaller than other samples, suggesting that doping-conductive polymer can modify significantly the electron transport and carriers, and hence improving the photocatalytic effect.
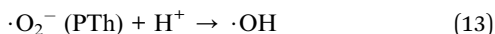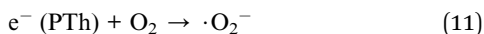
According to the literature research, the PTh/TiO_2 carrier mechanism conforms to the type II heterostructure,[36] that is, electrons flow from the LUMO level of PTh to the CB of TiO_2. Therefore, the introduction of GQDs regulated the band gap of TiO_2, resulting in the formation of a built-in electric field between GT and PTh, which promoted the outflow of electrons from TiO_2 CB and combined with the HOMO h^+ of PTh, thus maximized the retention of the REDOX capacity of the system and improved the catalytic performance.

Based on the experimental results, UV-vis DRS and VB XPS, the possible pollutant degradation mechanism of the efficient photocatalytic performance of the PTh/GT flexible fiber interface Z-scheme photocatalysts, is temporarily proposed and represented in Scheme 2. Previous studies have shown that the energy band position of PPy/GT is not enough to reduce the absorbed oxygen to $\cdot O_2^-$ most of the time after excitation of visible light. And likewise, $\cdot OH$ can't be formed on the HOMO. However, the band gap of PAn/GT is 1.23 eV. According to $E = 1240/\lambda$ (E is the band gap width, λ is the corresponding wavelength), its optical response range is only in the near infrared region. Therefore, the degradation capacity of PPy/GT and PAn/GT was weaker than that of PTh/GT. According to the literature research, the LUMO and HOMO of PTh are 0.45 and -1.50 eV, respectively.[71] In this case, PTh and GT have a good degree of relative energy-level matching, and chemical bonds interact

with one another and have a synergistic effect. GT can absorb visible light and produce an $e^-–h^+$ through excitation whereas PTh can absorb photons in visible light to induce $\pi–\pi^*$ transition, which moves electrons from the ground state to the excited state. In the case of a conventional heterostructure, electrons transfer from the LUMO of PTh to CB of GT; however, the CB potential of GT is insufficient to reduce adsorbed oxygen to $\cdot O_2^-$. Similarly, $\cdot OH$ cannot be made at the HOMO. Therefore, the Z-scheme heterojunction is better able to solve the electron transfer path of the catalytic system, that is, the migration of photogenerated electrons from CB of GT to HOMO of PTh. Electrons on the LUMO react to form $\cdot O_2^-$, and $\cdot O_2^-$ can react with H^+ to make a small amount of $\cdot OH$. In addition, the active sites retained on GT will also produce $\cdot OH$ to participate in degradation. The detailed reaction process is as follows (eqn (9)–(16)):

$$PTh + h\nu \rightarrow PTh \ (h^+/e^-) \tag{9}$$

$$GT + h\nu \rightarrow GT \ (h^+/e^-) \tag{10}$$
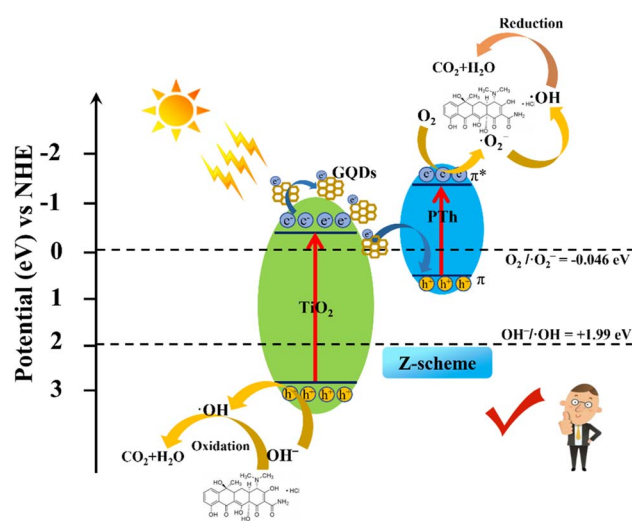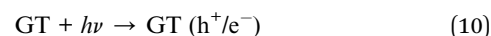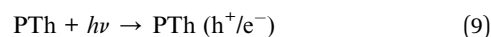
Scheme 2 Representation of interfacial charge separation at the PTh/GT heterojunction and free radical generation for TC degradation.

$$e^- \text{ (PTh)} + O_2 \rightarrow \cdot O_2^- \tag{11}$$

$$H_2O \rightarrow H^+ + OH^- \tag{12}$$

$$\cdot O_2^- \text{ (PTh)} + H^+ \rightarrow \cdot OH \tag{13}$$

$$OH^- + h^+ \text{ (GT)} \rightarrow \cdot OH \tag{14}$$

$$\cdot O_2^- + TC \rightarrow H_2O + CO_2 \tag{15}$$

$$\cdot OH + TC \rightarrow H_2O + CO_2 \tag{16}$$

4 Conclusions

In the present work, CPs/GQDs/TiO$_2$ flexible fiber membranes were synthesized by electrospinning and evaluated their photocatalytic performance under visible light. XRD, FTIR, TEM, and XPS spectra showed the effective synthesis of flexible fiber membrane, and there was a strong interaction between GT and PTh with electron transfer. The analysis of UV-vis DRS spectra showed that the light absorption range of a modified TiO$_2$-based photocatalyst was broadened to the entire visible light region. Furthermore, we demonstrate through various tests and experiments that the interfacial charge transfer mechanism of the catalytic system follows a Z-scheme heterojunction. The internal electric field established at the GT–PTh interface promotes the transfer of electrons in the GT CB to the PTh HOMO orbital and combines with the holes therein, effectively separating the electron–hole pairs of PTh and GT, preserving the excellent redox capacity. Therefore, the PTh/GT system showed the best photocatalytic performance. The degradation rates of PTh/GT hybrid fiber membranes were 4.06 and 1.70 times greater than those of TiO$_2$ and GT, in turn. In a word, we provide a new kind of highly efficient flexible TiO$_2$-based photocatalyst that can efficiently degrade contaminants and has excellent recycling performance and a good application prospect.

Conflicts of interest

There are no conflicts to declare.

Acknowledgements

Notes and references

1 S. P. Suresh, G. S. Lekshmi, S. D. Kirupha, M. Ariraman, O. Bazaka, I. Levchenko, K. Bazaka and M. Mandhakini, Superhydrophobic fluorine-modified cerium-doped mesoporous carbon as an efficient catalytic platform for photo-degradation of organic pollutants, *Carbon*, 2019, **147**, 323–333.

2 Y. P. Liu, S. J. Shen, J. T. Zhang, W. W. Zhong and X. H. Huang, Cu$_{2-x}$Se/CdS composite photocatalyst with enhanced visible light photocatalysis activity, *Appl. Surf. Sci.*, 2019, **478**, 762–769.

3 X. W. Huang, Y. Y. Li, M. T. M. Choi and X. Y. Li, Influence of high-strength permethrin and transfluthrin on biological wastewater treatment, *Chem. Eng. J.*, 2022, **442**, 136307.

4 C. F. Xia, H. H. Huang, D. Liang, Y. Xie, F. P. Kong, Q. H. Yang, J. X. Fu, Z. W. Dou, Q. Zhang and Z. L. Meng, Adsorption of tetracycline hydrochloride on layered double hydroxide loaded carbon nanotubes and site energy distribution analysis, *Chem. Eng. J.*, 2022, **443**, 136398.

5 J. Zhu, P. Z. Li, W. Guo, Y. Zhao and R. Zou, Titanium-based metal-organic frameworks for photocatalytic applications, *Coord. Chem. Rev.*, 2018, **359**, 80–101.

6 Y. Zhu, Y. Wang, Q. Ling and Y. Zhu, Enhancement of full-spectrum photocatalytic activity over BiPO$_4$/Bi$_2$WO$_6$ composites, *Appl. Catal., B*, 2017, **200**, 222–229.

7 Y. Wu, C. Liu, C. Wang, S. Lu and B. Zhang, Selective transfer semihydrogenation of alkynes with H$_2$O (D$_2$O) as the H (D) source over a Pd-P cathode, *Angew. Chem., Int. Ed.*, 2020, **59**, 21170–21175.

8 G. Yang, H. Yin, W. Liu, Y. Yang, Q. Zou, L. Luo, H. Li, Y. Huo and H. Li, Synergistic Ag/TiO$_2$-N photocatalytic system and its enhanced antibacterial activity towards acinetobacter baumannii, *Appl. Catal., B*, 2018, **224**, 175–182.

9 M. Pelaez, N. T. Nolan, S. C. Pillai, M. K. Seery, P. Falaras, A. G. Kontos, P. S. M. Dunlop, J. W. J. Hamilton, J. A. Byrne, K. O'Shea, M. H. Entezari and D. D. Dionysiou, A review on the visible light active titanium dioxide photocatalysts for environmental applications, *Appl. Catal., B*, 2012, **125**, 331–349.

10 Z. Y. Yao, H. J. Sun, S. B. Xiao, Y. L. Hu, X. F. Liu and Y. Zhang, Synergetic piezo-photocatalytic effect in a Bi$_2$MoO$_6$/BiOBr composite for decomposing organic pollutants, *Appl. Surf. Sci.*, 2021, **560**, 150037.

11 H. Li, M. R. Gadinski, Y. Huang, L. Ren, Y. Zhou, D. Ai, Z. Han, B. Yao and Q. Wang, Crosslinked fluoropolymers exhibiting superior high-temperature energy density and charge–discharge efficiency, *Energy Environ. Sci.*, 2020, **13**, 1279–1286.

12 E. M. Samsudin, S. B. Abd Hamid, J. C. Juan, W. J. Basirun and G. Centi, Synergetic effects in novel hydrogenated F-doped TiO$_2$ photocatalysts, *Appl. Surf. Sci.*, 2016, **370**, 380–393.

13 K. Wang, T. Peng, Z. Wang, H. Wang, X. Chen, W. Dai and X. Fu, Correlation between the H$_2$ response and its oxidation over TiO$_2$ and N doped TiO$_2$ under UV irradiation induced by Fermi level, *Appl. Catal., B*, 2019, **250**, 89–98.

14 H. Yu, H. Huang, K. Xu, W. Hao, Y. Guo, S. Wang, X. Shen, S. Pan and Y. Zhang, Liquid-Phase exfoliation into monolayered BiOBr nanosheets for photocatalytic

oxidation and reduction, *ACS Sustainable Chem. Eng.*, 2017, **5**, 10499–10508.

15 H. Safardoust-Hojaghan and M. Salavati-Niasari, Degradation of methylene blue as a pollutant with N-doped graphene quantum dot/titanium dioxide nanocomposite, *J. Cleaner Prod.*, 2017, **148**, 31–36.

16 S. Yan, S. Li, F. Xie, J. Wu, X. Jia, J. Yang, H. Song and Z. Zhang, Environmentally safe and porous MS@TiO$_2$@PPy monoliths with superior visible-light photocatalytic properties for rapid oil–water separation and water purification, *ACS Sustainable Chem. Eng.*, 2020, **8**, 5347–5359.

17 X. Wang, W. Cai, Y. Lin, G. Wang and C. Liang, Mass production of micro/nanostructured porous ZnO plates and their strong structurally enhanced and selective adsorption performance for environmental remediation, *J. Mater. Chem.*, 2010, **20**, 8582–8590.

18 Z. Wen, Y. Zhang, G. Cheng, Y. Wang and R. Chen, Simultaneous removal of As(V)/Cr(VI) and acid orange 7 (AO7) by nanosized ordered magnetic mesoporous Fe-Ce bimetal oxides: Behavior and mechanism, *Chemosphere*, 2019, **218**, 1002–1013.

19 A. Drenkova-Tuhtan, M. Schneider, M. Franzreb, C. Meyer, C. Gellermann, G. Sextl, K. Mandel and H. Steinmetz, Pilot-scale removal and recovery of dissolved phosphate from secondary wastewater effluents with reusable ZnFeZr adsorbent @ Fe$_3$O$_4$/SiO$_2$ particles with magnetic harvesting, *Water Res.*, 2017, **109**, 77–87.

20 R. Zhao, Y. Wang, X. Li, B. Sun, Y. Li, H. Ji, J. Qiu and C. Wang, Surface activated hydrothermal carbon-coated electrospun PAN fiber membrane with enhanced adsorption properties for herbicide, *ACS Sustainable Chem. Eng.*, 2016, **4**, 2584–2592.

21 M. Hu, X. Yan, X. Hu, J. Zhang, R. Feng and M. Zhou, Ultra-high adsorption capacity of MgO/SiO$_2$ composites with rough surfaces for Congo red removal from water, *J. Colloid Interface Sci.*, 2018, **510**, 111–117.

22 G. Duoerkun, Y. Zhang, Z. Shi, X. Shen, W. Cao, T. Liu, J. Liu, Q. Chen and L. Zhang, Construction of n-TiO$_2$/p-Ag$_2$O junction on carbon fiber cloth with Vis–NIR photoresponse as a filter-membrane-shaped photocatalyst, *Adv. Fiber Mater.*, 2020, **2**, 13–23.

23 M. Chen, C. Wang, W. Fang, J. Wang, W. Zhang, G. Jin and G. Diao, Electrospinning of calixarene-functionalized polyacrylonitrile nanofiber membranes and application as an adsorbent and catalyst support, *Langmuir*, 2013, **29**, 11858–11867.

24 D. H. Kang and H. W. Kang, Advanced electrospinning using circle electrodes for freestanding PVDF nanofiber film fabrication, *Appl. Surf. Sci.*, 2018, **455**, 251–257.

25 S. An, H. S. Jo, D. Y. Kim, H. J. Lee, B. K. Ju, S. S. Al-Deyab, J. H. Ahn, Y. Qin, M. T. Swihart, A. L. Yarin and S. S. Yoon, Self-junctioned copper nanofiber transparent flexible conducting film via electrospinning and electroplating, *Adv. Mater.*, 2016, **28**, 7149–7154.

26 T. Terao, C. Y. Zhi, Y. Bando, M. Mitome, C. C. Tang and D. Golberg, Alignment of boron nitride nanotubes in polymeric composite films for thermal conductivity improvement, *J. Phys. Chem.*, 2010, **114**, 4340–4344.

27 Q. Wang, S. Ji, Q. Xu, L. Shen and W. Shi, Preparation of PEO-based Cu$_2$O/Bi$_2$O$_2$CO$_3$ electrospun fibrous membrane toward enhanced photocatalytic degradation of chloramphenicol, *J. Mater. Sci.*, 2020, **56**, 4599–4614.

28 R. Zhang, Y. Ma, W. Lan, D. E. Sameen, S. Ahmed, J. Dai, W. Qin, S. Li and Y. Liu, Enhanced photocatalytic degradation of organic dyes by ultrasonic-assisted electrospray TiO$_2$/graphene oxide on polyacrylonitrile/beta-cyclodextrin nanofibrous membranes, *Ultrason. Sonochem.*, 2021, **70**, 105343.

29 L. Wang, Y. Wang, T. Xu, H. Liao, C. Yao, Y. Liu, Z. Li, Z. Chen, D. Pan, L. Sun and M. Wu, Gram-scale synthesis of single-crystalline graphene quantum dots with superior optical properties, *Nat. Commun.*, 2014, **5**, 5357–5366.

30 J. Zou, H. L. Yip, S. K. Hau and A. K. Y. Jen, Metal grid/conducting polymer hybrid transparent electrode for inverted polymer solar cells, *Appl. Phys. Lett.*, 2010, **96**, 203301.

31 M. Ates, M. El-Kady and R. B. Kaner, Three-dimensional design and fabrication of reduced graphene oxide/polyaniline composite hydrogel electrodes for high performance electrochemical supercapacitors, *Nanotechnology*, 2018, **29**, 175402.

32 C. J. Chang, Y. Y. Leong, C. F. Lai, W. Y. Chiou, M. J. Su and S. J. Chang, Performance of white light emitting diodes prepared by casting wavelength-converting polymer on InGaN devices, *J. Appl. Polym. Sci.*, 2017, **134**, 45210.

33 C. J. Chang, C. F. Lai, P. Madhusudhana Reddy, Y. L. Chen, W. Y. Chiou and S. J. Chang, Color optimization of conjugated-polymer/InGaN hybrid white light emitting diodes by incomplete energy transfer, *J. Lumin.*, 2015, **160**, 145–150.

34 C. F. Lai, C. J. Chang, C. L. Hsieh, Y. L. Chen and C. S. Tuan, Highly bright broadband red light produced by fluorescence polymer/InGaN hybrid light-emitting diodes, *Opt. Lett.*, 2013, **38**, 4082–4084.

35 S. L. Lee and C. J. Chang, Recent developments about conductive polymer based composite photocatalysts, *Polymers*, 2019, **11**, 206.

36 Y. Ma, Y. G. Xu, X. Y. Ji, M. Xie, D. Jiang, J. Yan, Z. L. Song, H. Xu and H. M. Li, Construction of polythiophene/Bi$_4$O$_5$I$_2$ nanocomposites to promote photocatalytic degradation of bisphenol a, *J. Alloys Compd.*, 2020, **15**, 153773.

37 L. E. Finch, M. M. Hillyer and M. C. Leopold, Quantitative Analysis of Heavy Metals in Children's Toys and Jewelry: A Multi-Instrument, Multitechnique Exercise in Analytical Chemistry and Public Health, *J. Chem. Educ.*, 2015, **92**, 849–854.

38 Y. Qiu, J. Lu, Y. Yan and J. Niu, Enhanced visible-light-driven photocatalytic degradation of tetracycline by 16% Er^{3+}-Bi$_2$WO$_6$ photocatalyst, *J. Hazard. Mater.*, 2022, **422**, 126920.

39 C. Zhou, J. Yan, B. Chen, P. Li, X. Dong, F. Xi and J. Liu, Synthesis and application of ternary photocatalyst with a gradient band structure from two-dimensional nanosheets as precursors, *RSC Adv.*, 2016, **6**, 108955–108963.

40 W. Li, D. Li, Y. Lin, P. Wang, W. Chen, X. Fu and Y. Shao, Evidence for the active species involved in the photodegradation process of methyl orange on TiO_2, *J. Phys. Chem. C*, 2012, **116**, 3552–3560.

41 S. Shang, X. Jiao and D. Chen, Template-free fabrication of TiO_2 hollow spheres and their photocatalytic properties, *ACS Appl. Mater. Interfaces*, 2012, **4**, 860–865.

42 S. Ding, F. Huang, X. Mou, J. Wu and X. Lu, Mesoporous hollow TiO_2 microspheres with enhanced photoluminescence prepared by a smart amino acid template, *J. Mater. Chem.*, 2011, **21**, 4888–4892.

43 Y. Wang, Q. Yang, G. Shan, C. Wang, J. Du, S. Wang, Y. Li, X. Chen, X. Jing and Y. Wei, Preparation of silver nanoparticles dispersed in polyacrylonitrile nanofiber film spun by electrospinning, *Mater. Lett.*, 2005, **59**, 3046–3049.

44 B. Santara, P. K. Giri, K. Imakita and M. Fujii, Evidence of oxygen vacancy induced room temperature ferromagnetism in solvothermally synthesized undoped TiO_2 nanoribbons, *Nanoscale*, 2013, **5**, 547654–547688.

45 A. Trapalis, N. Todorova, T. Giannakopoulou, N. Boukos, T. Speliotis, D. Dimotikali and J. Yu, TiO_2/graphene composite photocatalysts for NOx removal: A comparison of surfactant-stabilized graphene and reduced graphene oxide, *Appl. Catal., B*, 2016, **180**, 637–647.

46 H. C. Liang and X. Z. Li, Visible-induced photocatalytic reactivity of polymer–sensitized titania nanotube films, *Appl. Catal., B*, 2009, **86**, 8–17.

47 M. Li, Y. Guo, Y. Wei, A. G. MacDiarmid and P. I. Lelkes, Electrospinning polyaniline-contained gelatin nanofibers for tissue engineering applications, *Biomaterials*, 2006, **27**, 2705–2715.

48 Z. Lei, X. Sun, S. Zhu, K. Dong, X. Liu, L. Wang, X. Zhang, L. Qu and X. Zhang, Nature inspired MXene-decorated 3D honeycomb-fabric architectures toward efficient water desalination and salt harvesting, *Nano-Micro Lett.*, 2021, **14**, 10–26.

49 C. Lettmann, K. Hildenbrand, H. Kisch, W. Macyk and W. F. Maier, Visible light photodegradation of 4-chlorophenol with a coke-containing titanium dioxide photocatalyst, *Appl. Catal., B*, 2001, **32**, 215–227.

50 S. Sakthivel and H. Kisch, Daylight photocatalysis by carbon-modified titanium dioxide, *Angew. Chem., Int. Ed.*, 2003, **42**, 4908–4911.

51 Y. A. Liu, T. X. Zhang, R. Wang, *et al*, A facile and universal strategy for preparation of long wavelength emission carbon dots, *Dalton Trans.*, 2017, **46**, 16905–16910.

52 M. Zhang, Q. Hu, K. Ma, Y. Ding and C. Li, Pyroelectric effect in CdS nanorods decorated with a molecular Co-catalyst for hydrogen evolution, *Nano Energy*, 2020, **73**, 104810.

53 Y. Wang, W. Chu, S. Wang, Z. Li, Y. Zeng, S. Yan and Y. Sun, Simple synthesis and photoelectrochemical characterizations of polythiophene/Pd/TiO_2 composite microspheres, *ACS Appl. Mater. Interfaces*, 2014, **6**, 20197–20204.

54 M. Shen and H. Y. L. Chiou, Equilibrium and kinetic modeling of adsorption of reactive dye on cross-linked chitosan beads, *J. Hazard. Mater.*, 2002, **93**, 233–248.

55 Y. S. Ho and G. McKay, Sorption of dye from aqueous solution by peat, *Chem. Eng. J.*, 1998, **70**, 115–124.

56 Y. S. Ho and G. McKay, Pseudo-second order model for sorption processes, *Process Biochem.*, 1999, **34**, 451–465.

57 A. C. Zimmermann, A. Mecabo, T. Fagundes and C. A. Rodrigues, Adsorption of Cr(VI) using Fe-crosslinked chitosan complex (Ch-Fe), *J. Hazard. Mater.*, 2010, **179**, 192–196.

58 D. Pan, J. Jiao, Z. Li, Y. Guo, C. Feng, Y. Liu, L. Wang and M. Wu, Efficient separation of electron–hole pairs in graphene quantum dots by TiO_2 heterojunctions for dye degradation, *ACS Sustainable Chem. Eng.*, 2015, **3**, 2405–2413.

59 R. Li, L. Yu, X. Yan and Q. Tang, Efficient photocatalysts from polymorphic cuprous oxide/zinc oxide microstructures, *RSC Adv.*, 2015, **5**, 11917–11924.

60 P. Wang and Q. Yuan, Photocatalytic degradation of tetracyclines in liquid digestate: optimization, kinetics and correlation studies, *Chem. Eng. J.*, 2021, **410**, 128327.

61 M. Lei, N. Wang, L. Zhu, C. Xie and H. Tang, A peculiar mechanism for the photocatalytic reduction of decabromodiphenyl ether over reduced graphene oxide–TiO_2 photocatalyst, *Chem. Eng. J.*, 2014, **241**, 207–215.

62 A. Fujishima, X. Zhang and D. Tryk, TiO_2 photocatalysis and related surface phenomena, *Surf. Sci. Rep.*, 2008, **63**, 515–582.

63 Y. Sheng, Z. Wei, H. Miao, W. Yao, H. Li and Y. Zhu, Enhanced organic pollutant photodegradation via adsorption/photocatalysis synergy using a 3D g-C_3N_4/TiO_2 free-separation photocatalyst, *Chem. Eng. J.*, 2019, **370**, 287–294.

64 Y. Wang, M. K. Bayazit, S. J. A. Moniz, Q. Ruan, C. C. Lau, N. Martsinovich and J. Tang, Linker-controlled polymeric photocatalyst for highly efficient hydrogen evolution from water, *Energy Environ. Sci.*, 2017, **10**, 1643–1651.

65 P. Huo, P. Zhao, X. Shi, Z. Zhou and B. Liu, Enhanced photocatalytic performance of electrospun hollow titanium dioxide nanofibers decorated with graphene quantum dots, *J. Mater. Sci.*, 2020, **56**, 2138–2149.

66 G. Rajender, J. Kumar and P. K. Giri, Interfacial charge transfer in oxygen deficient TiO_2-graphene quantum dot hybrid and its influence on the enhanced visible light photocatalysis, *Appl. Catal., B*, 2018, **224**, 960–972.

67 C. Yang, N. Han, W. Zhang, W. Wang, W. Li, B. Xia, C. Han, Z. Cui and X. Zhang, Adhesive-free in situ synthesis of a coral-like titanium dioxide@poly(phenylene sulfide) microporous membrane for visible-light photocatalysis, *Chem. Eng. J.*, 2019, **374**, 1382–1393.

68 H. Liu, Z. G. Zhang, X. X. Wang, G. D. Nie, J. Zhang, S. X. Zhang, N. Cao, S. Y. Yan and Y. Z. Long, Highly flexible Fe_2O_3/TiO_2 composite nanofibers for photocatalysis and utraviolet detection, *J. Phys. Chem. Solids*, 2018, **121**, 236–246.

69 J. Zia, E. S. Aazam and U. Riaz, Highly efficient visible light driven photocatalytic activity of MnO_2 and Polythiophene/MnO_2 nanohybrids against mixed organic pollutants, *J. Mol. Struct.*, 2020, **1207**, 127790.

70 J. Wang and X. Ni, Photoresponsive polypyrrole-TiO$_2$ nanoparticles film fabricated by a novel surface initiated polymerization, *Solid State Commun.*, 2008, **146**, 239–244.

71 J. Zhang, H. Bi, G. He, Y. Zhou and H. Chen, Fabrication of Ag$_3$PO$_4$−PANI−GO composites with high visible light photocatalytic performance and stability, *J. Environ. Chem. Eng.*, 2014, **2**, 952–957.

72 S. H. Xu, S. Y. Li, Y. X. Wei, L. Zhang and F. Xu, Improving the photocatalytic performance of conducting polymer polythiophene sensitized TiO$_2$ nanoparticles under sunlight irradiation, *React. Kinet., Mech. Catal.*, 2010, **101**, 237–249.

73 G. L. Xu, M. L. Du, T. Li, Y. P. Guang and C. Guo, Facile synthesis of magnetically retrievable Fe$_3$O$_4$/BiVO$_4$/CdS heterojunction composite for enhanced photocatalytic degradation of tetracycline under visible light, *Sep. Purif. Technol.*, 2021, **275**, 119157.

74 Y. Deng, L. Tang, G. Zeng, J. Wang, Y. Zhou, J. Wang, J. Tang, L. Wang and C. Feng, Facile fabrication of mediator-free Z-scheme photocatalyst of phosphorous-doped ultrathin graphitic carbon nitride nanosheets and bismuth vanadate composites with enhanced tetracycline degradation under visible light, *J. Colloid Interface Sci.*, 2018, **509**, 219–234.

75 Y. Zeng, N. Guo, H. Li, Q. Wang, X. Xu, Y. Yu, X. Han and H. Yu, Construction of flower-like MoS$_2$/Ag$_2$S/Ag Z-scheme photocatalysts with enhanced visible-light photocatalytic activity for water purification, *Sci. Total Environ.*, 2019, **659**, 20–32.

76 Z. Liang, J. Li, N. Lei, L. Guo and Q. Song, Construction of Ti^{3+} self-doped TiO$_2$/BCN heterojunction with enhanced photoelectrochemical performance for water splitting, *J. Mater. Sci.: Mater. Electron.*, 2018, **30**, 2006–2015.

77 H. Zhang, X. Quan, S. Chen, H. Yu and N. Ma, "Mulberry-like" CdSe nanoclusters anchored on TiO$_2$ nanotube arrays: A novel architecture with remarkable photoelectrochemical performance, *Chem. Mater.*, 2009, **21**, 3090–3095.

78 L. Yang, L. Huang, Y. Yao and L. Jiao, In-situ construction of lattice-matching NiP$_2$/NiSe$_2$ heterointerfaces with electron redistribution for boosting overall water splitting, *Appl. Catal., B*, 2021, **282**, 119584.